LASER POWDER BED FUSION PARAMETER DRIVEN POROSITY FOR 15-5 PH

Lappeenranta–Lahti University of Technology LUT

Master's Programme in Mechanical Engineering, Master's Thesis

2026

Leo Lintukangas

Examiners: Dosent Ilkka Poutiainen

Sami Westman, M.Sc. (Tech.)

ABSTRACT

Lappeenranta–Lahti University of Technology LUT

LUT School of Energy Systems

Mechanical Engineering

Leo Lintukangas

Laser Powder Bed Fusion Parameter Driven Porosity For 15-5 PH

Master's thesis

2026

52 pages, 31 figures and 2 tables

Examiners: Dosent Ilkka Poutiainen and Sami Westman, M.Sc. (Tech.)

Keywords: L-PBF, porosity, parameter driven porosity, programmed porosity, VED, AM

This Master's thesis studies parameter driven porosity in Laser Powder Bed Fusion (L-PBF) for 15-5 PH stainless steel. Typical L-PBF additive manufacturing focuses on maximizing part density and minimizing defects. Parameter driven porosity opens novel applications for printed parts, such as filtration and flow control systems. The primary objective is to achieve a controllable relationship between specific process parameters and the resulting internal pore characteristics.

Test specimens are manufactured with an EOS M280 system by modifying key process parameters: hatch spacing, scanning speed, and laser spot size. The printed parts are evaluated through Scanning Electron Microscopy (SEM) imaging, geometric porosity measurements, gas permeability testing and mechanical testing.

The results demonstrated that increasing the hatch distance significantly increases the total porosity (which ranged from 5.8% to 23.5% across the tested parameters) and average pore size, while predictably reducing the mechanical strength of the part. Notably, the gas permeability did not directly correlate with the total geometric porosity. The largest hatch spacings led to overhang collapse and closed sidewall pores, which restricted airflow. Furthermore, increased scanning speeds induced severe balling effects, causing high deviations in pore geometry, while a reduced laser spot size created narrow, deep pores and heavily sealed sidewalls.

The study concludes that utilizing highly porous L-PBF components in the as-built state yields unpredictable permeability due to un-melted powder trapped inside the complex internal channels. Developing and applying effective post-processing powder removal methods is essential for utilizing L-PBF porous parts in functional industrial applications.

TIIVISTELMÄ

Lappeenrannan–Lahden teknillinen yliopisto LUT

LUTin energiajärjestelmien tiedekunta

Konetekniika

Leo Lintukangas

Parametriohjattu huokoisuus 15–5 PH-teräksen laser-jauhepetisulatuksessa

Konetekniikan diplomityö

2026

52 sivua, 31 kuvaa ja 2 taulukkoa

Tarkastajat: Dosentti Ilkka Poutiainen ja DI Sami Westman

Avainsanat: L-PBF, huokoisuus, tarkoituksellinen huokoisuus, VED, AM

Tämä diplomityö tutkii prosessiparametrien avulla ohjattua huokoisuutta 15–5 PH ruostumattoman teräksen jauhepeti (L-PBF) 3D-tulostuksessa. Tyypillinen L-PBF perustuva 3D-metallitulostus keskittyy kappaleiden tiheyden maksimoimiseen ja valmistusvirheiden minimoimiseen. Parametrien avulla ohjattu huokoisuus avaa tulostetuille osille uusia sovelluskohteita, kuten suodatin- ja virtauksensäätöjärjestelmiä. Päätavoitteena on määrittää hallittava yhteys tiettyjen prosessiparametrien ja niistä muodostuvien sisäisten huokosominaisuuksien välille. Koekappaleet valmistettiin EOS M280 -laitteistolla muokkaamalla keskeisiä prosessiparametreja: laserin väliä, skannausnopeutta ja laserin säteen kokoa. Tulostettuja osia kuvattiin pyyhkäisyelektronimikroskoopilla (SEM), geometrisilla huokoisuusmittauksilla, kaasunläpäisevyystesteillä ja mekaanisilla kokeilla.

Tulokset osoittivat, että viivavälin kasvattaminen lisää merkittävästi kokonaishuokoisuutta (joka vaihteli 5,8 % ja 23,5 % välillä) ja keskimääräistä huokoskokoa, samalla kun se heikentää kappaleen mekaanista lujuutta. Huomionarvoista oli, ettei kaasunläpäisevyys korreloinut suoraan geometrisen kokonaishuokoisuuden kanssa. Suurimmat viivavälit johtivat sularadan romahtamiseen ja sivuseinämien huokosten sulkeutumiseen, mikä rajoitti ilmavirtausta. Lisäksi korkeammat skannausnopeudet aiheuttivat palloutumista (balling), mikä johti suureen hajontaan huokosgeometriassa. Pienempi laserin säteen koko puolestaan loi kapeita, syviä huokosia ja tiiviisti sulkeutuneita sivuseinämiä. Tutkimuksen johtopäätöksenä todetaan, että voimakkaasti huokoisten L-PBF-komponenttien käyttö sellaisenaan (as-built) johtaa arvaamattomaan läpäisevyyteen monimutkaisten sisäisten kanavien sisälle jäävän sulamattoman pulverin vuoksi. Tehokkaiden pulverinpoistomenetelmien kehittäminen ja soveltaminen on välttämätöntä, jotta L-PBF-menetelmällä valmistettuja huokoisia osia voidaan hyödyntää toiminnallisissa teollisissa sovelluksissa.

ACKNOWLEDGEMENTS

I want to express my thanks to Materflow, which made it possible to carry out this thesis. They gave me a great opportunity to learn more about such an interesting topic and were really helpful throughout this project. I would also like to express my thanks to my thesis examiners, Ilkka and Sami, who helped me move forward with this thesis. They also helped me carry out the tests at LUT University, which was a very nice experience.

Special thanks go to my family, who have been supporting me throughout this whole journey. Biggest thanks to Sonja, who helped me keep going forward all the time through this thesis process.

SYMBOLS AND ABBREVIATIONS

Roman characters

A	cross-sectional area	mm^2, m^2
E_v	VED	$\mathrm{J/mm}^3$
F	force	N
H	hatch spacing	mm
L	thickness	m
P	laser power	W
p	pressure	Pa
Q	volumetric airflow	m^3/s
V	volume	m^3
v	scanning speed	mm/s

Greek characters

δ	layer thickness	µm
κ	permeability	m^2
ρ	density	$\mathrm{kg/m}^3$
σ	normal stress	Mpa

Constants

µ	dynamic viscosity of air	$1{,}82 \cdot 10^{-5}\ \mathrm{Pa} \cdot \mathrm{s}$

Abbreviations

L-PBF	Laser Powder Bed Fusion
AM	Additive Manufacturing
VED	Volumetric Energy Density
LoF	Lack of Fusion
SEM	Scanning Electron Microscopy
NDT	Non-Destructive Testing
DoE	Design of Experiment
UTS	Ultimate Tensile Strength

Table of contents

Abstract

Acknowledgements

Symbols and abbreviations

Declarations

1 Introduction 6
1.1 Background and previous work 6
1.2 Research problem of the study 7
1.3 Scope and Implementation 7
2 L-PBF and Theoretical Framework for Porosity Control 8
2.1 Laser Powder Bed Fusion 8
2.2 Porosity in L-PBF 9
2.2.1 Unintentional Porosity 10
2.2.2 Intentional Porosity 12
2.3 Parameters affecting porosity 13
2.3.1 Laser power and melt pool 13
2.3.2 Hatch spacing and scanning strategy 14
2.3.3 Scanning speed 16
2.3.4 Other process parameters 16
2.4 Summary of the possible process parameters for parameter driven porosity 16
3 Experimental phase 18
3.1 Printing setup 18
3.1.1 15-5 PH 18
3.2 Printing parameters of the specimen 19
3.3 Printing of the specimens 20
3.4 Preparing specimens for testing 23
3.5 Testing of the specimens 24
4 Results 27

4.1 SEM images of porous specimens 27
4.2 Porosity of the specimen 33
4.3 Permeability measurement 35
4.4 Mechanical test results 35
5 Discussion 38
5.1 Combining mechanical results with porosity 38
5.2 Combining permeability with porosity 39
5.3 Effect of as-built state into results 41
5.4 Build orientation effect to porosity 41
5.5 Reliability of the test results 42
5.6 Further research topics 42
6 Conclusions 43
References 44

Figures

Figure 1. L-PBF process. (Armstrong, M. et al. 2022)

Figure 2. Main parameters of L-PBF (Chowdhury, S. et al. 2022)

Figure 3. LBP-F fabricated part with lack of fusion pore. (Buhairi, M. A. et al. 2023)

Figure 4. Keyhole pore formation (Du, C. et al. 2023)

Figure 5. Balling defect simulated with different scanning speeds. (Wang, W., Ning, J., & Liang, S. Y. 2021)

Figure 6. Effect of process parameters to porosity of 3d printed part in horizontal orientation

Figure 7. Calculated melt pool dimensions for Inconel 625 with parameters: P = 270 W, v = 1000 mm/s and t = 40 μm. (Letenneur, M. et al. 2019)

Figure 8. Optical micrograph of porous parts. Hatch distances (a) h = 0.140 mm (b) h = 0.155 mm (c) h = 0.170 (d) h = 0.185 (e) h = 0.200 mm (f) = 0.215 mm (Zhang, L. et al. 2025)

Figure 9. Different scan patterns (Calignano, F. 2018)

Figure 10. SEM specimens in magics software

Figure 11. Tensile specimen dimensions

Figure 12. Compression specimen dimensions

Figure 13. Filter specimen dimensions

Figure 14. Porous specimens after printing

Figure 15. Permeability test setup

Figure 16. Tensile test setup

Figure 17. SEM images from parameter 1 specimen

Figure 18. SEM images from parameter 4 specimen

Figure 19. SEM images from parameter 5 specimen

Figure 20. SEM images from parameter 8 specimen

Figure 21. SEM images from parameter 11 specimen

Figure 22. Comparison of air blasted and as built specimen

Figure 23. Comparison of heat treated and as built specimen

Figure 24. Bar chart of average pore size with standard deviation

Figure 25. Total porosity of the specimens

Figure 26. Permeability test results

Figure 27. Stress-strain curves for all specimens

Figure 28. Compressive stress-strain curves

Figure 29. Maximum displacement of compression specimens.

Figure 30. Total porosity vs Ultimate Tensile Strength

Figure 31. Total porosity with gas permeability

Tables

Table 1. 15-5 PH chemical composition (Oerlikon. 2026)

Table 2. L-PBF process parameters

DECLARATIONS

Turnitin

The originality of this thesis has been reviewed with the Turnitin similarity checking service.

AI usage

The author of the thesis, Leo Lintukangas, used the following AI-tools during the preparation of the thesis:

1. AI tool name Microsoft Copilot
    a. Purpose of use: Translation
    b. Explanation of the use of the tool: This AI tool was used to assist in English translations.
2. AI tool name Google Gemini
    a. Purpose of use: MATLAB code generating, improving clarity of the text.
    b. Explanation of the use of the tool: This AI tool was used to generate MATLAB code for making calculations and drawing charts. This AI tool was used to improve word choices in text and to improve sentences into more understandable text.

Responsibility

The author, Leo Lintukangas, takes full responsibility for the content of this thesis and has reviewed and edited the content generated by the possible use of AI tools.

1 Introduction

This master's thesis studies parameter driven porosity in Laser Powder Bed Fusion metal additive manufacturing for 15-5 PH. The primary objective is to establish a controllable relationship between process parameters and pore characteristics. Various testing methods are used to gain verification of the pore structure. Typical L-PBF additive manufacturing focuses on maximizing density and minimizing defects such as porosity, due to its negative effect on part mechanical properties. Programmed porous structures are achieved by modifying process parameters to influence the printed part structure. There is variety of applications for porous AM parts, such as filters and flow control for programmed porous AM parts.

This study is conducted in collaboration with Materflow, a commercial 3D printing service provider for industrial customers specializing in custom plastic and metal components. Materflow provided the materials and manufactured all the test specimens required for this research.

1.1 Background and previous work

This thesis is continuation of Materflow's internal research on porous structures. which has remained partially incomplete. In the current metal AM market, only a few companies offer programmed porous parts. These components have the potential to become highly valuable products if the correct pore characteristics and permeability can be reliably achieved and verified.

In their earlier studies, Materflow experimented with CAD-modelled porosity as well as porosity based on known L-PBF defect modes. The main challenges encountered with these early specimens were verifying the actual pore size and addressing the issue of un-melted powder trapped inside the pore channels. Additionally, internal balance and structural integrity of the porous parts require further validation. Parameter driven porosity is still a relatively new field in metal additive manufacturing and there is limited number of academic studies focusing parameter driven porosity.

1.2 Research problem of the study

The primary research problem of the study is to identify the optimal printing parameters to produce controlled porosity. There is no straight model that connects specific L-PBF process parameters to specific controlled pore type. The limitations from the previous preliminary work specimens needs to be minimized. The verification of the printed porous structures must be conducted using appropriate testing methods and equipment. Specific pore shape and size need to be linked to the corresponding process parameters. The effect of the process parameters to the pore structure can be validated after printing and testing of the specimens.

There are two research questions, which must be answered to solve the research problem. Research questions of the study are:

- Which specific parameters result the intended pore characteristics?
- How the chosen parameters result the pore structure?

1.3 Scope and Implementation

The scope of the study is limited to a single material 15-5 PH stainless steel. The test specimens are manufactured using EOS M280 L-PBF system with 400W fiber laser. Two different laser spot size of 75 µm and smaller than 75 µm are used. Effect of the main parameters are studied to gain control over the resulting porosity.

The research utilizes a Design of Experiment (DoE) methodology. Suitable parameters for achieving desired pore sizes are initially defined based on existing scientific literature. In experimental phase several test specimens are printed with Materflow's EOS M280 printer using the parameters found from the theoretical framework. The specimens are prepared for analysis, which is conducted at the LUT University Laser and Additive Manufacturing laboratory. Scanning Electron Microscope (SEM) imaging, gas permeability testing and mechanical testing is performed to determine if the desired pore structure is achieved.

2 L-PBF and Theoretical Framework for Porosity Control

In this chapter Metal Additive Manufacturing Method L-PBF is presented. Solutions for achieving parameter driven porosity are also presented in this chapter.

2.1 Laser Powder Bed Fusion

L-PBF is used to produce high-precision and complex additively manufactured metal parts. Part sizes are generally relatively small, as they are physically restricted by the specific machine's build volume. Parts are manufactured by melting pre-spread metal powder with a laser. The laser scanning path is defined to follow the cross-sectional geometry of the part in each layer. At the beginning of the printing process, the metal powder melts into a thin layer that attaches to the build plate (substrate). When one layer is completed, the substrate lowers by one layer height and a recoater spreads another layer of metal powder. The subsequent layers melt into the previous ones. This process continues until the part is finished. (Armstrong, M. et al.2022)

Figure 1 illustrates L-PBF process along with machine part names. An inert gas, such as nitrogen or argon is used inside the build chamber to prevent oxidation.

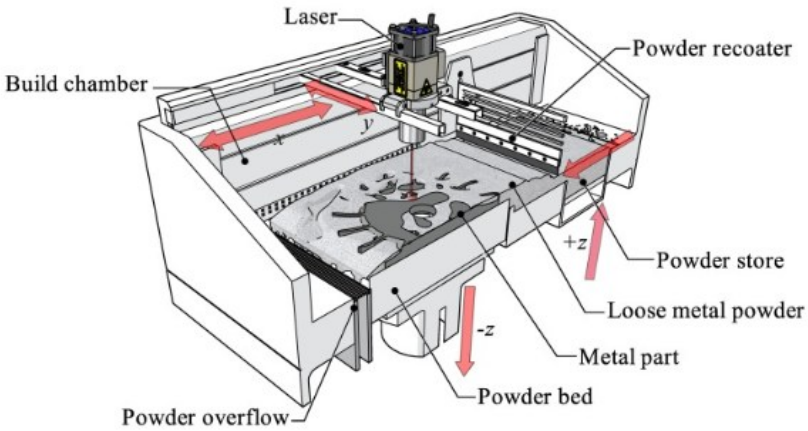

Figure 1. L-PBF process. (Armstrong, M. et al. 2022)

Volumetric Energy Density (VED) is one of the key factors in L-PBF. It describes the ability of the laser to melt metal powder. Higher energy density means that more heat is concentrated into melt pool, which leads to a deeper penetration. Equation for Volumetric Energy Density

$$E_v = \frac{P}{V\delta H} \quad (1)$$

Where E_v is VED (J/mm^3), P is laser power (W), V is scanning speed (mm/s), δ is layer thickness (µm) and H is hatch spacing (mm). These are main parameters in L-PBF that can be modified to adjust the printed part, whether aiming for a fully dense structure or parameter driven porosity. Figure 2 illustrates location of the main parameters during printing. (Sardarian, S. et al. 2024)

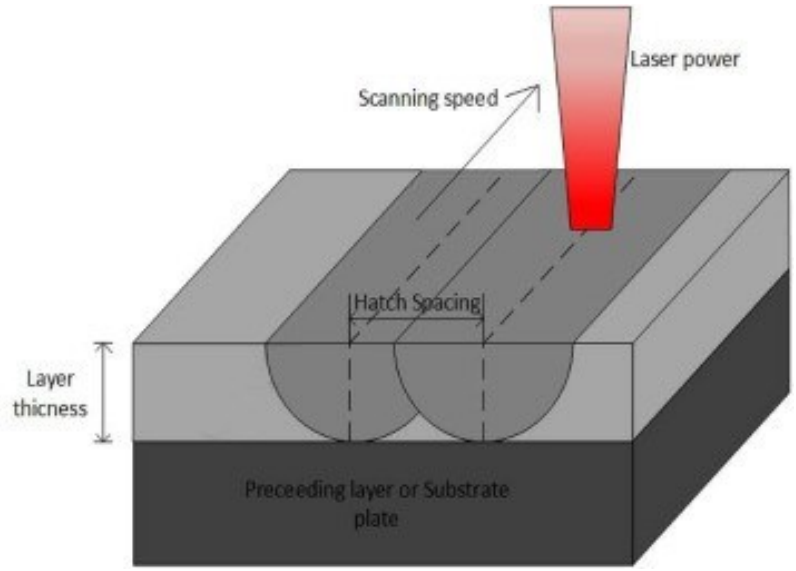

Figure 2. Main parameters of L-PBF (Chowdhury, S. et al. 2022)

2.2 Porosity in L-PBF

Pores are the most significant defects in L-PBF and are usually minimize due to their negative effect on a part's mechanical properties. Typically, parts are manufactured to be as dense as possible, but nowadays porous parts are developed to gain specific functional

advantages. Pores can occur inside the prints or on the surface, depending on the process parameters, material quality and defect mechanisms. (Brennan, M. C. et al. 2021)

2.2.1 Unintentional Porosity

The pores that most frequently occur in L-PBF are Lack of Fusion (LoF) and gas type pores, which includes keyhole collapse. LoF is one of the most common pore formation mechanisms in L-PBF. It occurs when the energy density and the overlap of the laser scan paths are insufficient. The metal powder does not melt completely, creating irregular and sharp pores that can sometimes trap un-melted powder, as shown in Figure 3. This defect can be controlled by adjusting hatch spacing and laser power, which affect the scan path overlap and the width of the melt pool. LoF can also occur at the layer level when the melt pool is too low to penetrate the previous layer, leading to incomplete metallurgical bonding between layers. (Du, C. et al. 2023)

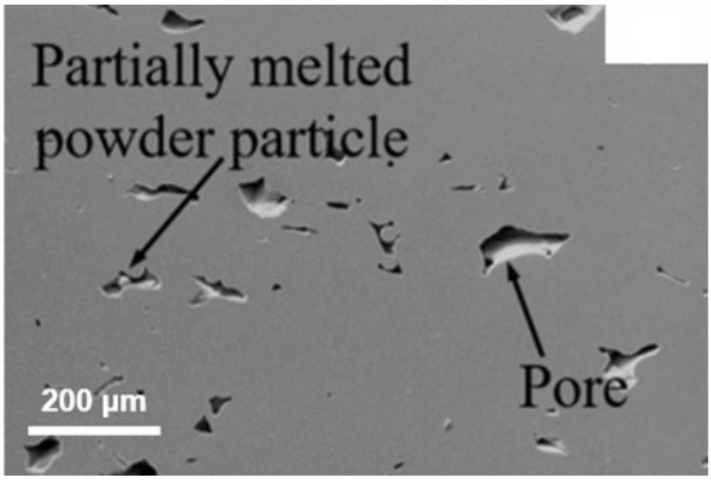

Figure 3. LBP-F fabricated part with lack of fusion pore. (Buhairi, M. A. et al. 2023)

Keyhole collapse is a gas-type pore defect that occurs when the energy density is excessively high. Keyhole pore formation starts with a deep V-shaped melt pool, leading to rapid and highly localized melting of the powder. Metal vapor ejects upwards, and the keyhole collapses, creating voids with trapped vapor inside (Brennan, M. C. et al. 2021). Figure 4 illustrates the formation of a keyhole pore. Keyhole pores are difficult to control due to their

instability and tendency to fluctuate and collapse, making them undesirable for generating intentional porosity (Du, C. et al. 2023).

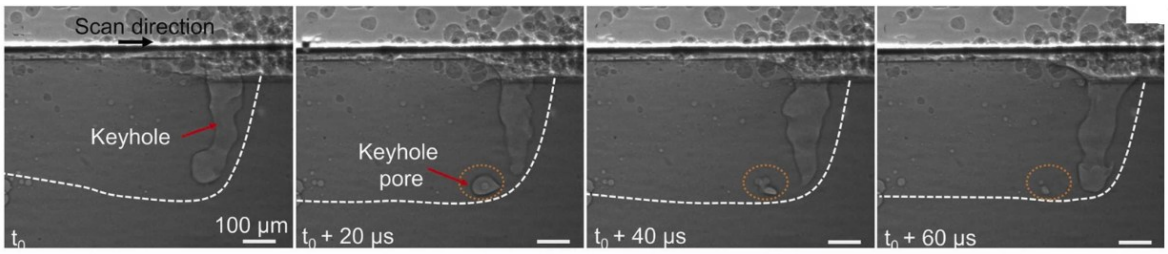

Figure 4. Keyhole pore formation (Du, C. et al. 2023)

Another defect mode that causes porosity is balling. Balling is primarily caused by poor wetting between solidified layers when energy density is too low due to high scanning speed or low laser power. This causes the melt track to break up, leading to pore formation and potentially uneven powder spreading in the next layer. Figure 5 illustrates influence of scanning speed to severity of balling. If controlled properly, the balling effect can be utilized to create random pore gaps. (Wang, W., Ning, J., & Liang, S. Y. 2021).

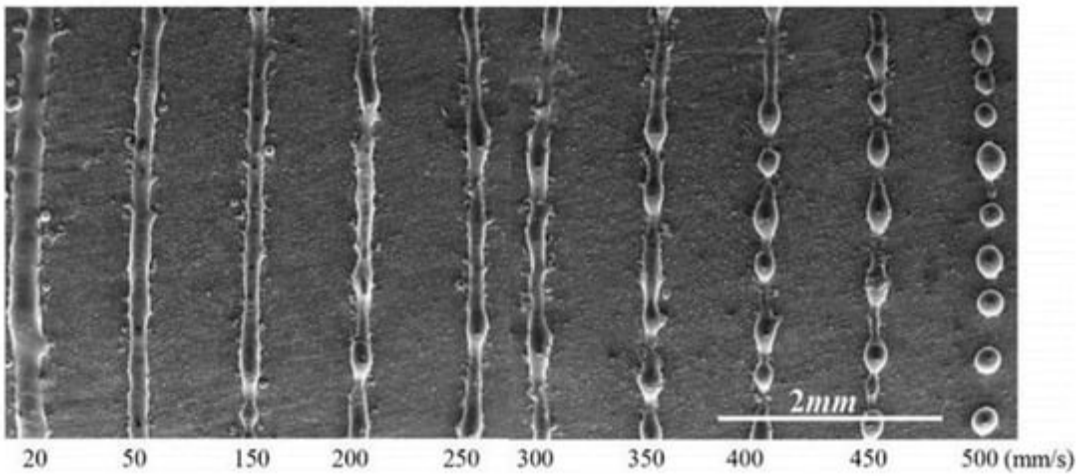

Figure 5. Balling defect simulated with different scanning speeds. (Wang, W., Ning, J., & Liang, S. Y. 2021)

2.2.2 Intentional Porosity

Although pores are defects, their intentional fabrication can provide valuable benefits for printed parts and open new application areas for printed parts. For example, successfully produced porous parts can be used for flow control, filtration, dampening, mixing and heat exchange. (Guddati, S. et al. 2019)

Parameter driven porosity can be achieved by adjusting the parameters that VED includes and leveraging existing knowledge of porosity defect mechanisms. By managing the VED, the melting of the metal powder can be reduced while preserving good structural integrity. This allows for increased porosity while still maintaining suitable mechanical properties. (Haiati, S. et al. 2025)

Figure 6a illustrates an optimal dense structure, where scan paths overlap sufficiently to fully melt the metal powder into a solid part. By modifying specific parameters, intentional porosity can be created, as shown in Figure 6b. An ideal porous part has small gaps between laser tracks that prevent the powder from fully melting into a dense structure, creating interconnected pores in both the horizontal and vertical directions.

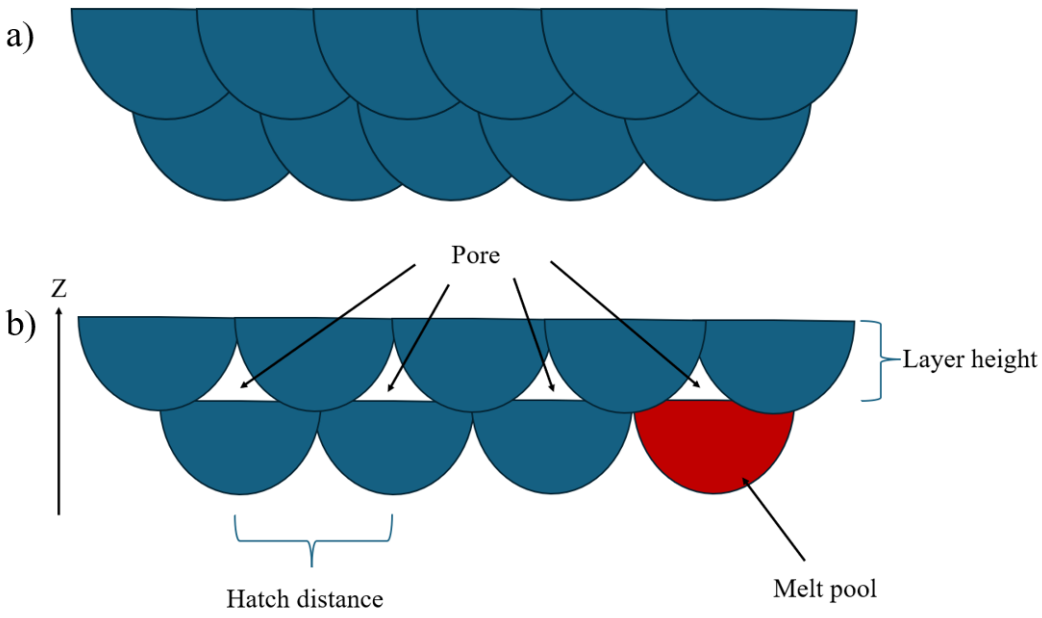

Figure 6. Effect of process parameters to porosity of 3d printed part in horizontal orientation

2.3 Parameters affecting porosity

In this section, the main process parameters affecting parameter driven porosity are examined in more detail. Typically, hatch distance, laser power, scan speed and layer thickness are primary parameters to be modified. The effects of the scanning strategy and laser spot size are also examined.

2.3.1 Laser power and melt pool

Laser power is one of the primary parameters controlling the penetration and melting of the metal powder. Insufficient laser power can prevent the metal powder from melting completely, resulting in LoF type pores. Usage of too high laser power leads to high penetration and typically results in keyhole type pores. (Buhairi, M. A. et al. 2023)

Keeping the laser power at the lower limit with insufficient overlap results in elongated pores oriented both horizontally and vertically due to insufficient melting. By maintaining a consistent VED and controlling of the melt pool, unwanted keyhole pores can be mitigated. (Vaglio, E. et al. 2024) Figure 7 illustrates the calculated dimensions of the melt pool for Inconel 625. As seen in the Figure 7 the melt pool shape is gaussian beam type, with the deepest penetration in middle of the melt pool.

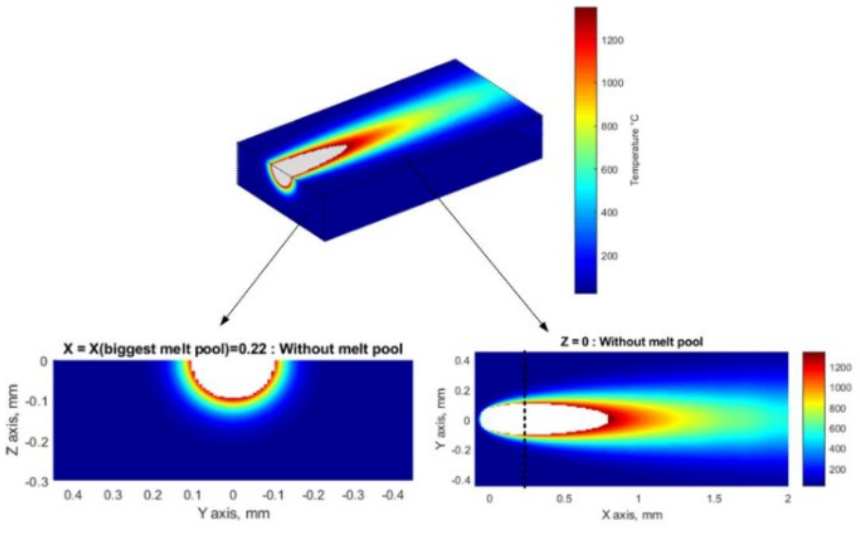

Figure 7. Calculated melt pool dimensions for Inconel 625 with parameters: P = 270 W, v = 1000 mm/s and t = 40 μm. (Letenneur, M. et al. 2019)

2.3.2 Hatch spacing and scanning strategy

Hatch distance has one of the biggest effects on the permeability, size and type of the porosity. It means distance between laser scan paths. Using wider hatch distances that are over 0.13 mm combined with low laser power greatly increases porosity and permeability of the part, while also increasing surface roughness. Pores form between the solidified scan paths as well as within them. With smaller hatch distances, the gaps between the scanned paths are minimized and the overall size of the pores is reduced. (Xie, D. & Dittmeyer, R. 2021)

Intentional porosity can be achieved by setting the hatch distance wider than the melt track width. This configuration eliminates the overlap between adjacent tracks, intentionally leaving un-scanned gaps that act as designed pore channels. Additionally, the scanning angle is typically rotated between layers so that the melt channels cross, creating interconnected pore channels along the building direction. Figure 8 illustrates straight effect of hatch distance to size of porosity. (Zhang, L. et al. 2025)

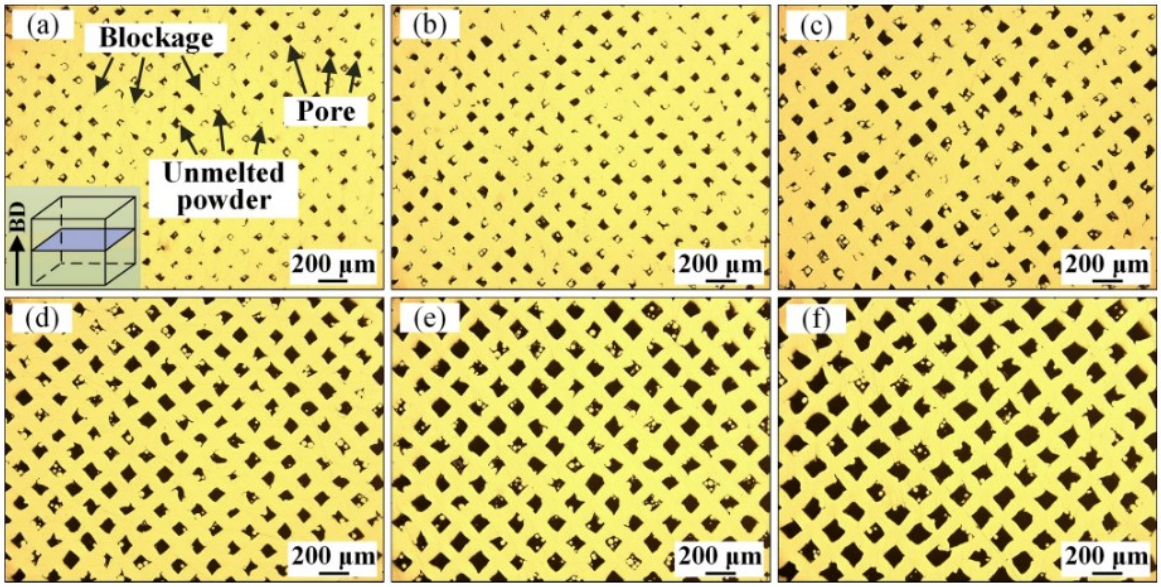

Figure 8. Optical micrograph of porous parts. Hatch distances (a) h = 0.140 mm (b) h = 0.155 mm (c) h = 0.170 (d) h = 0.185 (e) h = 0.200 mm (f) = 0.215 mm (Zhang, L. et al. 2025)

Different scanning strategies can also be used to influence the pore type and the overall permeability of the part. The scan direction for each layer is modified to achieve these advantages. Figure 9 show five common scan strategy patterns for L-PBF. These strategies are often combined with a larger hatch spacing to generate a porous structure. (Calignano, F. 2018)

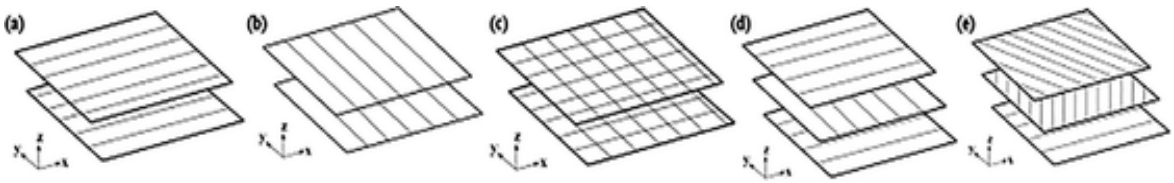

Figure 9. Different scan patterns (Calignano, F. 2018)

2.3.3 Scanning speed

Scanning speed also plays an important role during printing, as it directly affects the part's microstructure and density. Balling defects typically occur when using a high scanning speed combined with low laser power. With too low scanning speed, the energy density rises significantly, creating distortion and irregularities such as keyhole pores. (Buhairi, M. A. et al. 2023)

The optimal scanning speed is highly dependent on the laser power used. The VED can be lowered by increasing the scan speed, which leads to a more porous part due to insufficient melting. (Vaglio, E. et al. 2024)

2.3.4 Other process parameters

The laser spot size affects the concentration of the laser energy. Increasing the laser spot size tends to decrease the pore size and permeability of the part. A larger spot size distributes the energy over a wider area, causing less intense melting of the powder, which causes powder to attach the surface. This increases roughness on the surface. (Xie, D. & Dittmeyer, R. 2021)

Layer height is another crucial component of VED, typically ranging from 20 to 50 μm. Using a layer height that is too high results in incomplete melting of the powder bed. It also affects the dimensional accuracy of the part and can cause balling defects. While thinner layers improve product quality and mechanical properties, they significantly increase the build time. Too small layer height leads to increase of the VED, which can cause keyhole porosity due to deep penetration and excessive melting. (Buhairi, M. A. et al. 2023)

2.4 Summary of the possible process parameters for parameter driven porosity

Parameter driven porous structures are going to be made by modifying hatch spacing mostly. Layer height, laser power and scan speed needs only small modifications or can be held constant just as making normal prints. Laser spot can be changed if it is possible. Desired hatch spacing around 0.13-0.2 mm to make porous structure, but it also depends on the other

process parameters. To prevent part to fully melt, hatch spacing distance needs to be at least diameter of laser spot size. Scanning speed is used about range of 800-1000 mm/s. It can't be too high to prevent severe balling. Finally, the scanning direction is rotated 90° for each subsequent layer to generate a grid-like structure, which facilitates the formation of interconnected pore channels.

3 Experimental phase

In this chapter, parameter driven porosity is tested based on the parameter findings from the literature review. The printing setup is further introduced, detailing the material and the specific parameters used.

3.1 Printing setup

The specimens are printed using an EOS M280 Laser Powder Bed Fusion machine equipped with a maximum laser power of 400 W and a build volume of 250 x 250 x 325 mm. The standard laser spot size used is 75 µm, though a spot size smaller than 75 µm is also tested. To achieve this, the laser spot size is manually adjusted one click smaller using the physical controller on the EOS printer. Nitrogen gas is used in the build chamber to prevent the oxidation of the printed parts.

3.1.1 15-5 PH

The material used in this study is 15-5 PH stainless steel. The main properties of the 15-5 PH are good corrosion resistance and excellent mechanical properties, such as high hardness and strength. It is mostly used in medical, aerospace and other demanding engineering applications. The chemical composition for 15-5 PH is presented in Table 1. (Oerlikon. 2026)

Table 1. 15-5 PH chemical composition (Oerlikon. 2026)

Fe	Cr	Ni	Cu	Nb	C
77,1 %	14,5 %	4,5 %	3,5 %	0,3 %	< 0,07 %

The nominal particle size range of the metal powder is 15 – 45 µm. Specifically, 90% of the particles are under size if the 50 µm, 50 % of the particles are under size 33 µm, and 10 % of the particles are under size of the 20 µm. (Oerlikon. 2026)

3.2 Printing parameters of the specimen

EOS recommended parameters for producing a fully dense structure are used with modified hatch spacing and laser spot size. The specimens are printed with 12 different parameters sets. Table 2 presents the specific parameters used for each specimen in this study. For specimens 9-12 exact laser spot size is not known, but it is confirmed to be smaller than 75 µm. A scanning strategy alternating between the x and y directions, with a 90° rotation for each subsequent layer is used when printing.

Table 2. L-PBF process parameters

Parameter ID	Laser power (W)	Hatch distance (mm)	Scan speed (mm/s)	Layer thickness (µm)	Laser spot size (µm)
1	195	0,130	800	40	75
2	195	0,150	800	40	75
3	195	0,170	800	40	75
4	195	0,190	800	40	75
5	195	0,130	1000	40	75
6	195	0,150	1000	40	75
7	195	0,170	1000	40	75
8	195	0,190	1000	40	75
9	195	0,130	800	40	<75
10	195	0,150	800	40	<75
11	195	0,170	800	40	<75
12	195	0,190	800	40	<75
EOS	195	0,1	800	40	75

3.3 Printing of the specimens

Size of 5 x 5 x 5 mm cubes are printed for Non-Destructive Testing (NDT). The specimens are printed using the 12 different parameters sets. Each cube is printed twice.

Support structures for the specimen are generated in Magics software, before importing print file to the printer as Figure 10 illustrates. A 5 mm thick block-type support structure is used to provide sufficient space for cutting the specimen off the substrate without damaging the porous structure.

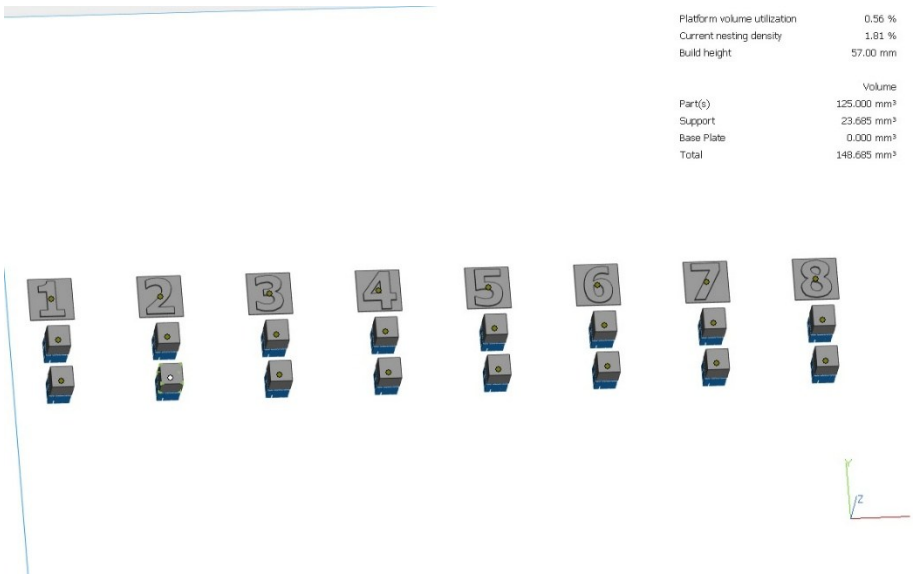

Figure 10. SEM specimens in magics software

The cross-sectional dimensions of the tensile and compression test specimens are specifically modelled so that the parts would break or yield before the testing machine reached its maximum force capacity of 10 kN. The equation for normal stress is

$$\sigma = \frac{F}{A} \tag{2}$$

Where σ is tensile strength (MPa), F is force (N) and A is cross-sectional area (mm^2).

The ultimate tensile strength of 15-5 PH is approximately 1300 MPa for fully dense heat-treated structure (Oerlikon, 2026). The tensile test specimen is modelled according to the ASTM E8/E8M – 13a standard for sub-size specimens and cross-section dimensions are modified by using Equation (2) to meet suitable values. The dimensions of the end sections of the specimen are increased to prevent possible slipping in the test grips. The tensile specimen is printed in the vertical z-direction. Supports are generated on the rounded sections of the part, as they contained minor overhangs. The final dimensions for the tensile specimen are shown in Figure 11.

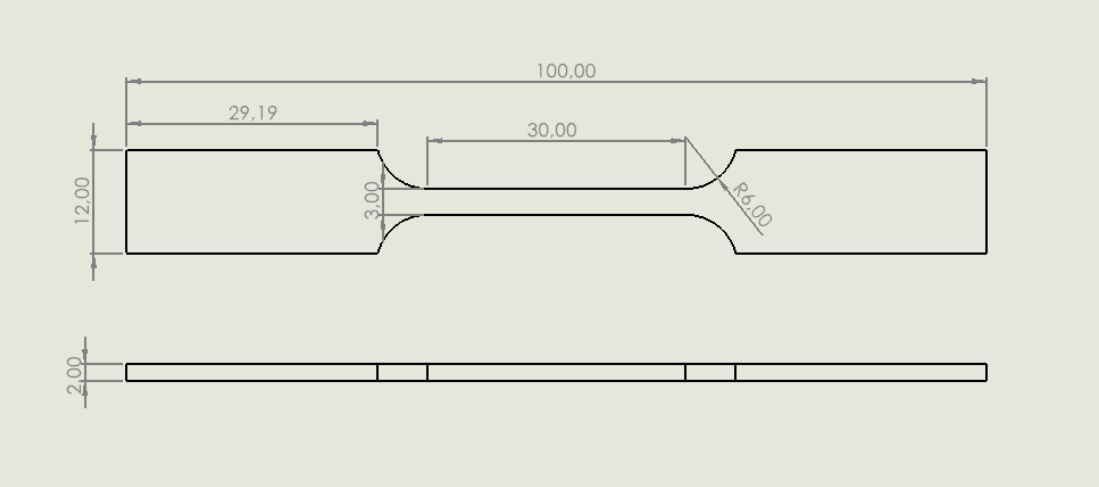

Figure 11. Tensile specimen dimensions

The compression test is carried out for cylinder shaped specimen with diameter of 4 mm and height of 10 mm. Same machine with maximum of 10 kN is used to compress specimen. Figure 12 illustrates shape and dimensions for compression test specimen.

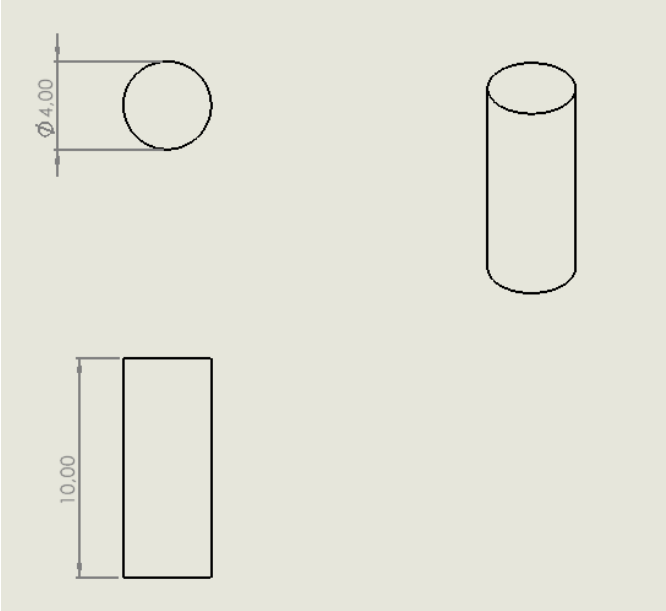

Figure 12. Compression specimen dimensions

The filter specimen is modelled into shape of circular disc with diameter of 54 mm and thickness of 3 mm to fit specimens into permeability test rig. Figure 13 illustrates the dimensions and shape of filter specimen. Filter specimens are printed upright (vertically) to prevent pores to get filled with metal when removing supports.

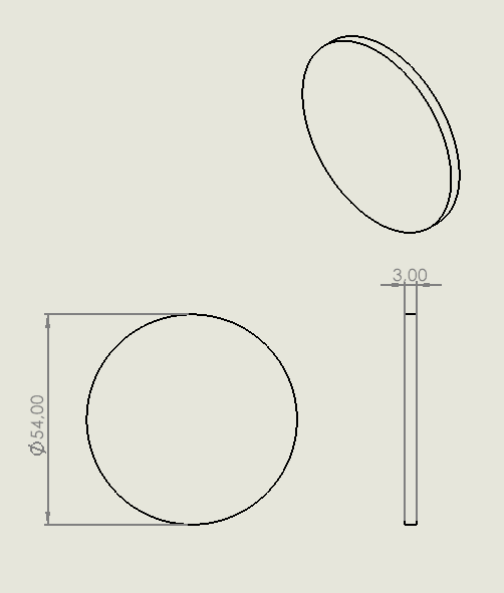

Figure 13. Filter specimen dimensions

3.4 Preparing specimens for testing

After the prints are finished, the specimens are removed from the M280 printer and vacuumed fully from loose metal powder. The specimens are cut from the substrate using a bandsaw. Figure 14 shows the substrate with printed the printed porous parts before removal.

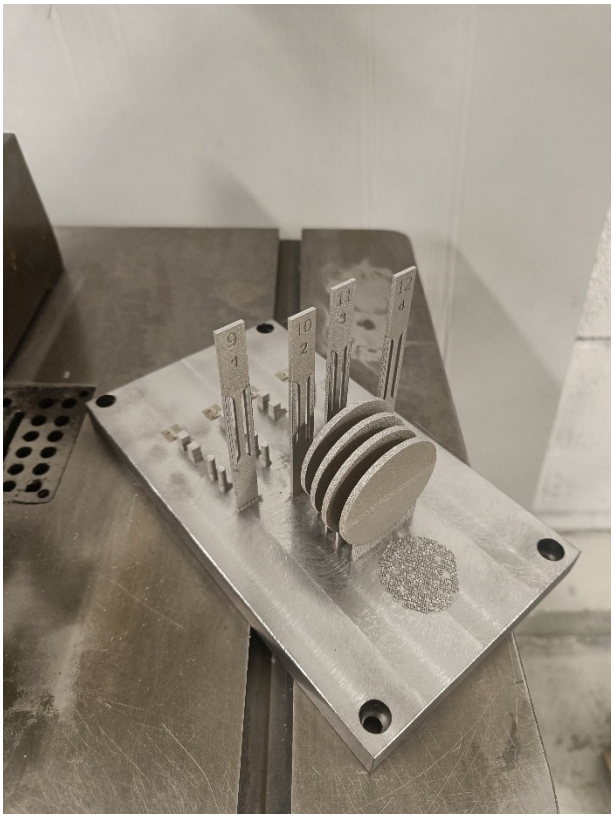

Figure 14. Porous specimens after printing

H900 heat treatment for 1 hour is carried out for half of the SEM specimens, as H900 is a standard heat treatment for 15-5 PH material. This is done to observe any potential changes in the porous structure through SEM imaging, particularly to see if loose powder particles would fuse or attach more firmly to the walls of the porous structure.

3.5 Testing of the specimens

All tests for the specimens are performed in the as-built condition unless specified otherwise.

The SEM images are taken in the LUT-University Chemical Engineering laboratory using a Hitachi SU3500 Scanning Electron Microscope. SEM cube specimen's top surface and sidewall is captured to see how porosity appears across different areas of the cubes. Due to SEM time constraints, only a portion of the specimens are being captured. The selected specimens are chosen to provide an approximate overview of the effects of the varying process parameters.

Pore sizes are measured from the SEM images using the ImageJ application, utilizing the scale bar provided in the SEM images. Visual pores on both the side and top surfaces are measured to determine the average pore size. Total porosity is determined by weighing the filter specimens on a scale with accuracy of 0,5 g. The measured weights are compared to the calculated weight of a fully solid part with the same dimensions. The equation used to calculate the total porosity is

$$Total\ porosity\ (\%) = \left(1 - \frac{\rho_{measured}}{\rho_{theoretic}}\right) \cdot 100 \quad (3)$$

Where ρ is density (kg/m^3).

The gas permeability test is conducted in the LUT-University Chemical Engineering laboratory. All support structures are removed from the specimens before testing. The test is performed by passing airflow through porous specimens in a room temperature. The change in airflow resulting from the pressure drop is recorded. Based on these measurements, the permeability of the specimens is calculated using Darcy's law. Equation for Darcy's law is

$$\kappa = \frac{Q \cdot \mu \cdot L}{A \cdot \Delta P} \quad (4)$$

Where κ is permeability (m^2), Q is volumetric airflow (m^3/s), μ is dynamic viscosity of air ($Pa \cdot s$), L is thickness of specimen (m), A is cross-sectional area of the specimen (m^2), ΔP is difference in pressure (Pa). (Guddati, S. et al. 2019)

Test setup is shown in Figure 15. The specimen is securely clamped between modified steel pliers equipped with a sealing ring. Additional tape is applied around the edges to ensure no air leaked during the measurement.

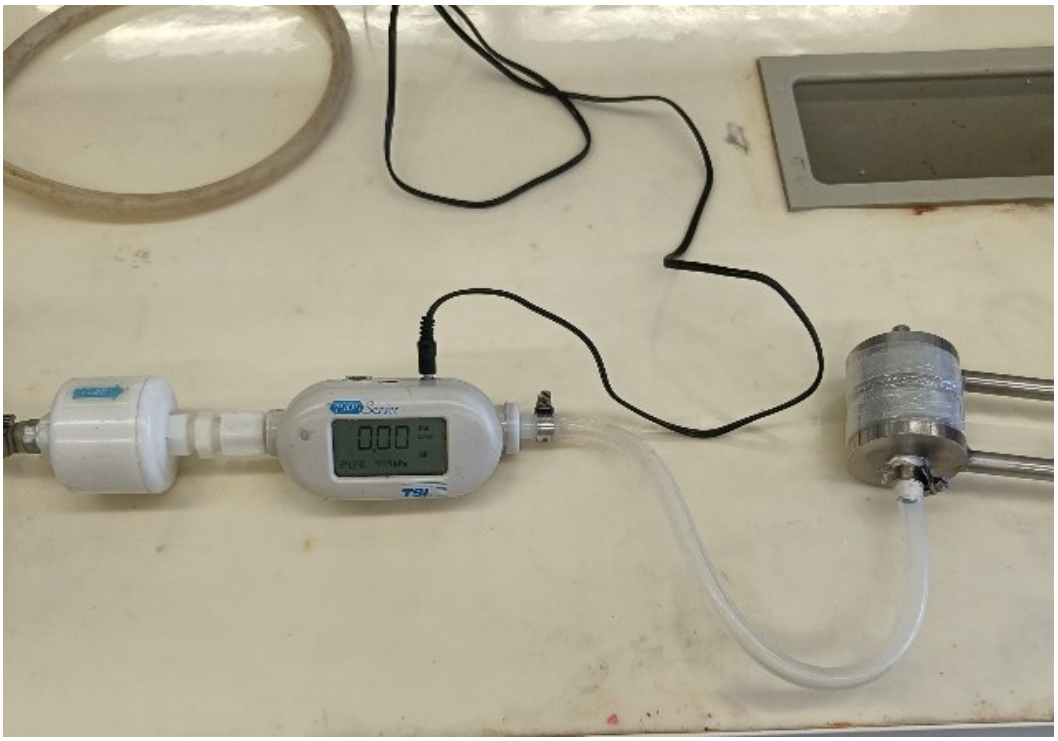

Figure 15. Permeability test setup

The tensile test is conducted in the LUT-University Laser material processing and additive manufacturing laboratory. All support structures are removed from the specimens before testing. Test is carried out using an MTS Systems universal testing machine with maximum force of 10 kN. The tensile test setup is shown in Figure 16.

Figure 16. Tensile test setup

Compression test is performed with same MTS machine as in the tensile test. The tool head is changed for suitable to conduct compression test. The machine maximum force is limited to 9 kN to prevent machine getting stuck.

4 Results

In this chapter, the results from the various tests are presented. MATLAB is utilized to generate visual charts for the different data sets to assist in presenting and interpreting the results.

4.1 SEM images of porous specimens

Pores can be observed as dark regions in the SEM images, representing variations in surface depth. The rounded shapes and spheres indicate loose or partially attached metal powder particles.

The SEM images of the parameter set 1 specimen, shown in Figure 17, display only a few small pore gaps. The VED is highest in parameter set 1. More pores are visible on the top surface compared to the sidewall. A significant amount of loose or partially sintered metal powder can be observed on the sidewall.

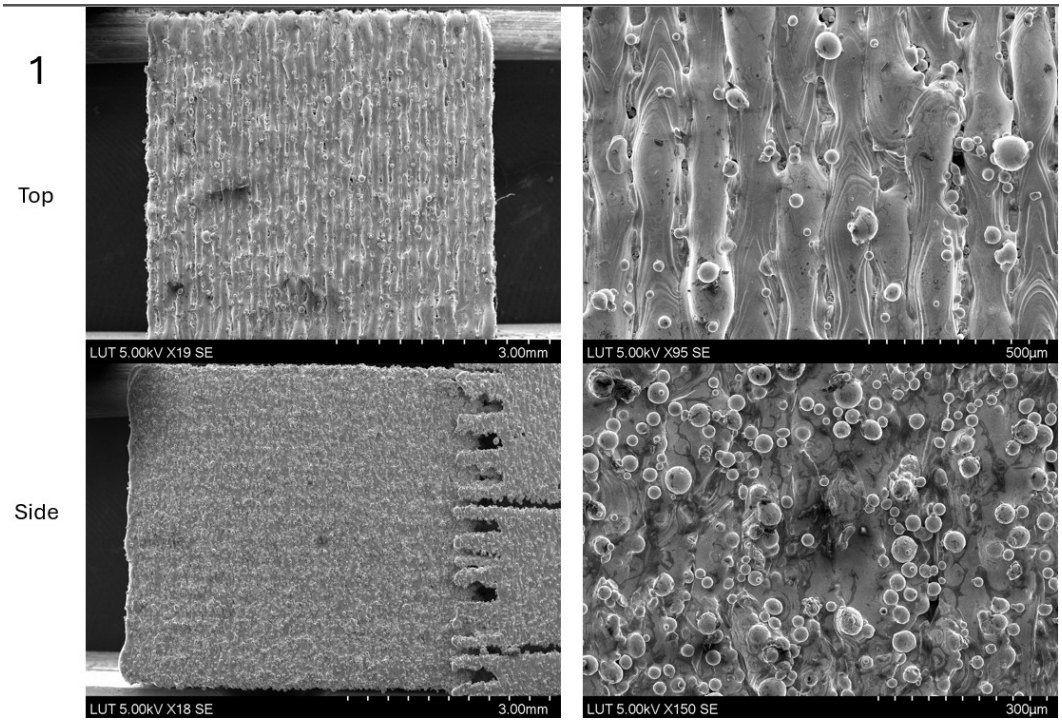

Figure 17. SEM images from parameter 1 specimen

Parameter 4 SEM images in Figure 18 demonstrate that the laser tracks do not overlap as much as they do in the parameter set 1 image. The hatch distance is increased from 0.13 mm to 0.19 mm. With this increased hatch distance, more pores can be observed in the SEM images. Only the top surface is captured.

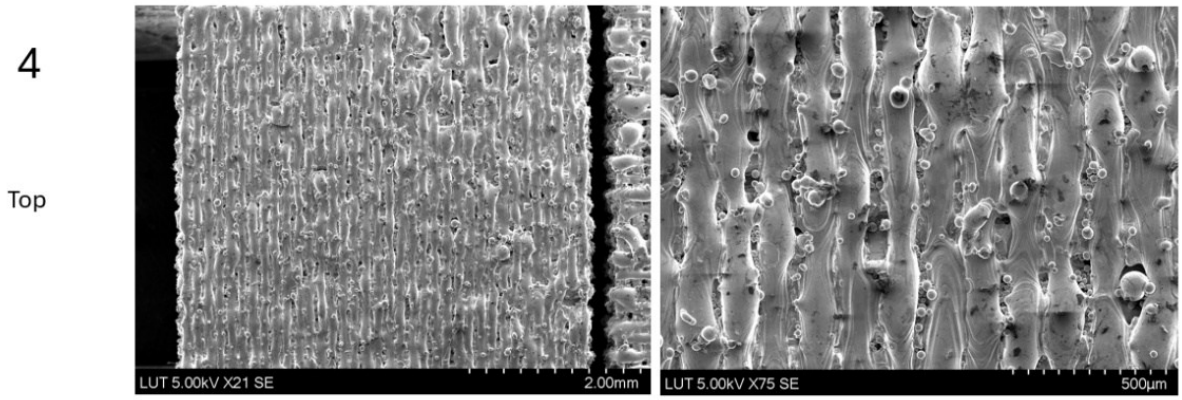

Figure 18. SEM images from parameter 4 specimen

Parameter 5 SEM images in Figure 19 indicate a higher level of porosity compared to the specimens from parameter sets 1 and 4. The balling phenomena occurs on the top surface because the laser melt track is discontinuous and breaks up randomly. Even though the hatch spacing is narrowest value 0,13 mm, the laser melted tracks do not overlap.

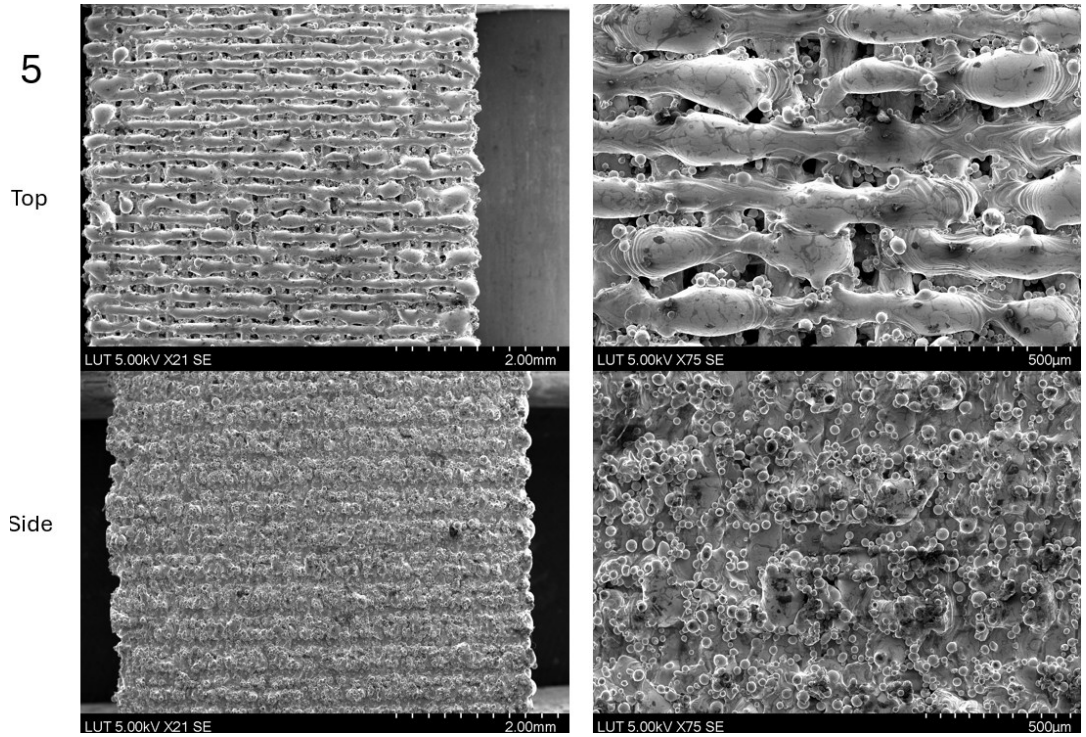

Figure 19. SEM images from parameter 5 specimen

Parameter set 8 SEM images in Figure 20 shows balling phenomena similar to parameter set 5 SEM images. The laser melt track is unstable and periodically breaks up. Due to the increased hatch distance compared to parameter set 5, the pore gaps are slightly larger. The scanning strategy formed a grid-like structure, which successfully created pore gaps between the melt tracks as intended.

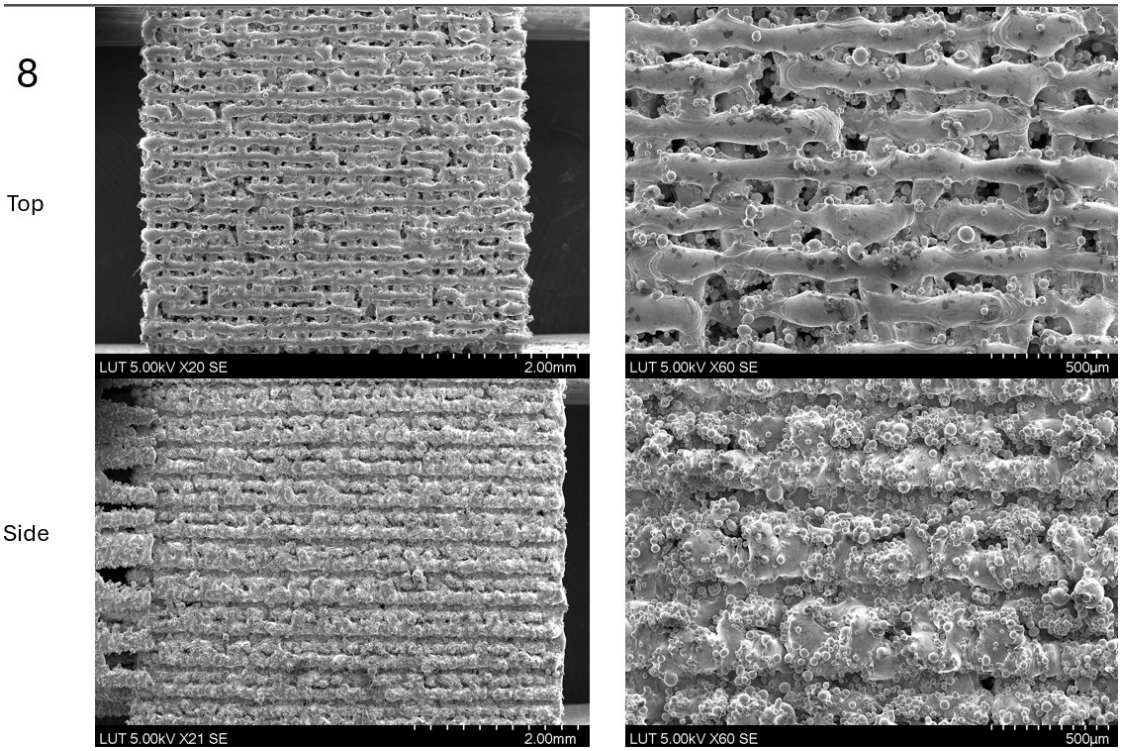

Figure 20. SEM images from parameter 8 specimen

Parameter set 11 SEM images in Figure 21, which utilized a smaller laser spot under 75 µm shows very closed sidewall structure. A smaller laser spot size concentrates the energy, causing deeper penetration and forcing the sidewall structure to melt shut. The top-side SEM images indicate that the laser melt track is narrower than in the previous parameter sets. Pore channels from the top surface appear narrow and deep.

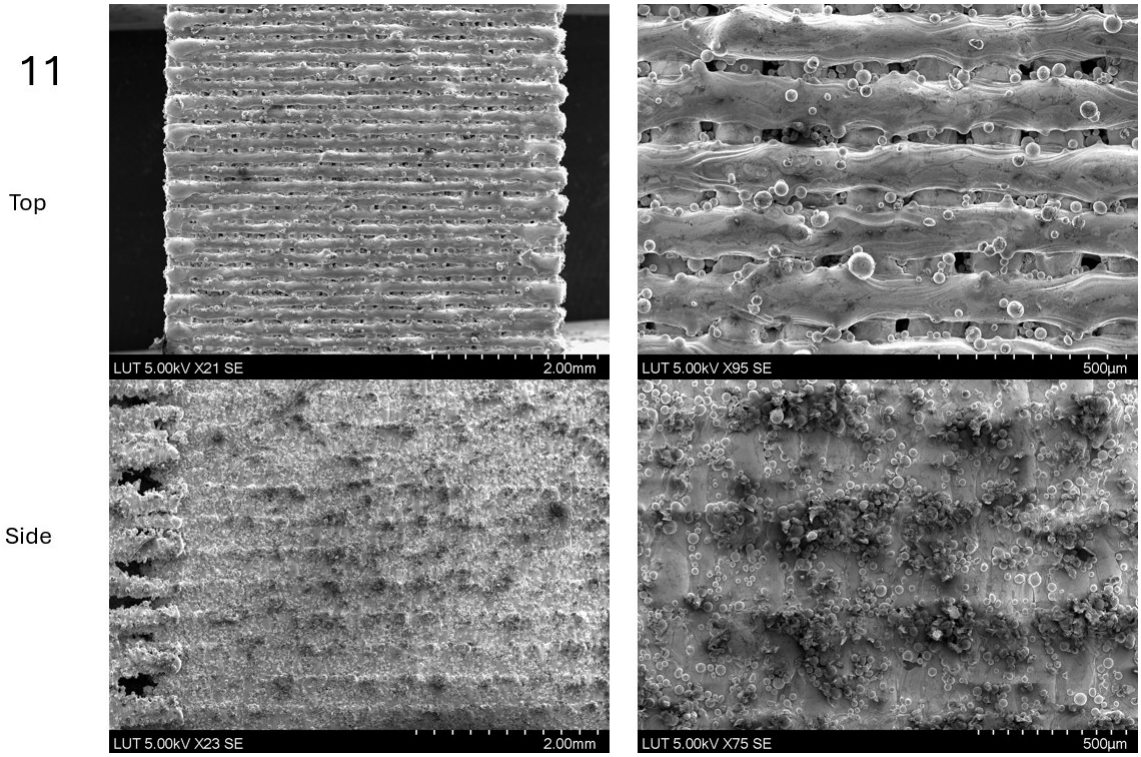

Figure 21. SEM images from parameter 11 specimen

Overall, a substantial amount of loose or partially sintered powder is heavily present in all SEM images. For comparison, additional SEM images of the top surface of specimen 8 are captured. One specimen is cleaned with compressed air, and another is heat-treated. Figure 22 shows loose powder is cleared from the surface by the air blast, the sintered or partially sintered metal powder particles remained firmly attached to the part's surface.

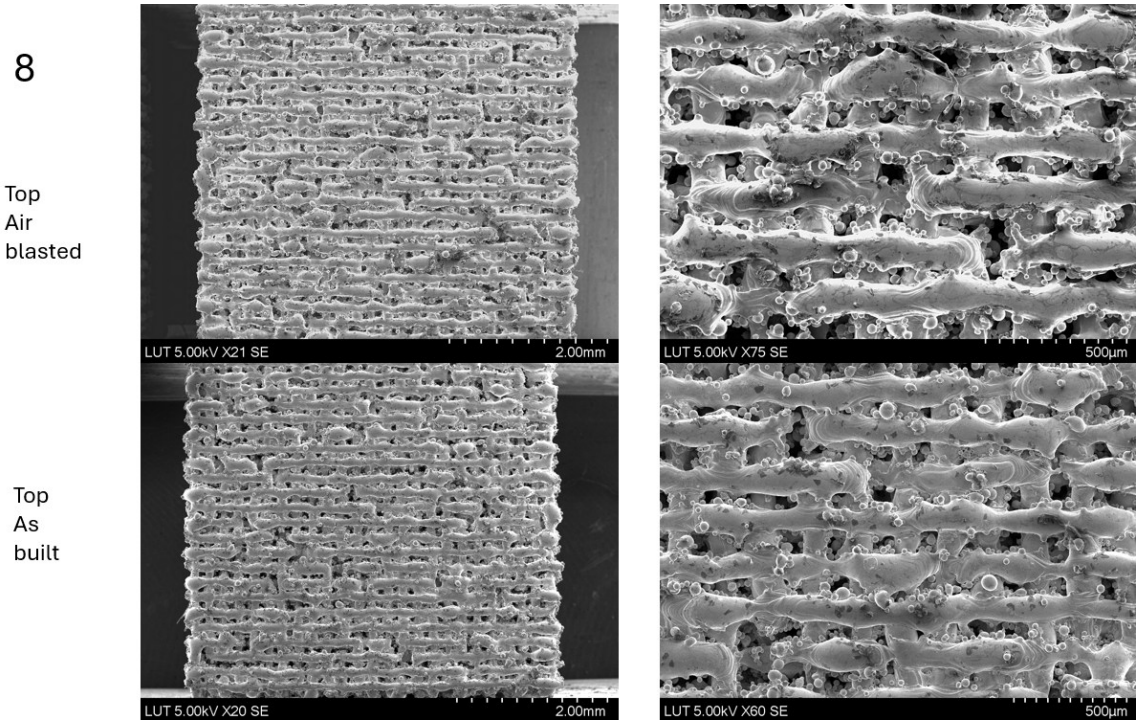

Figure 22. Comparison of air blasted and as built specimen

The effect of heat treatment on the surface structure is observed to be very minimal. Based on the Figure 23 SEM images, it is difficult to determine whether the loose powder has attached to the walls. The H900 heat-treatment temperature is far below the melting point of 15-5 PH, so the powder is unlikely to have bonded any better.

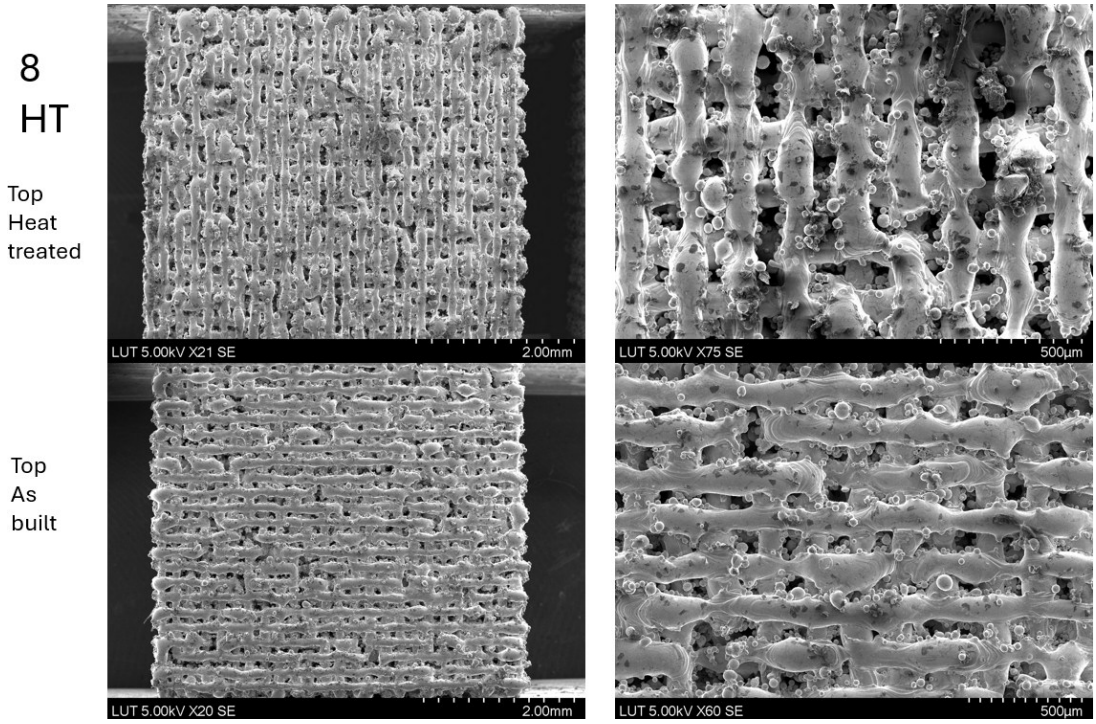

Figure 23. Comparison of heat treated and as built specimen

4.2 Porosity of the specimen

The average pore sizes measured from the SEM images are presented in Figure 24. The pore size is clearly larger on the top surface compared to the side surface. Notably, the pores on the top surface of specimen 8 exhibit a large standard deviation. This indicates that the balling effect leads to larger and more randomized pore sizes.

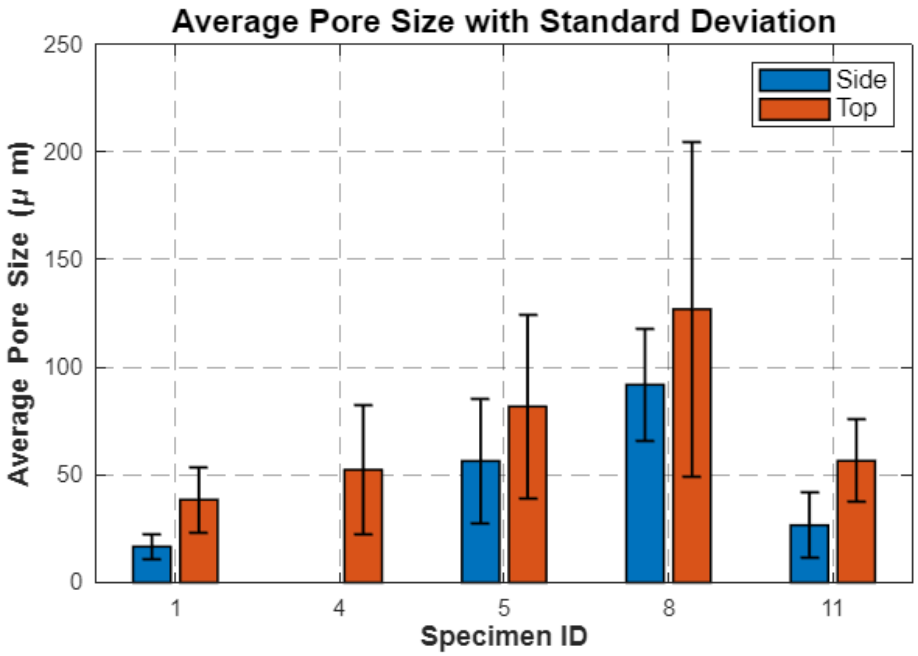

Figure 24. Bar chart of average pore size with standard deviation

The geometrically measured total porosity of the 12 different specimens is illustrated in Figure 25. Specimens 4, 8, and 12, which are manufactured with the largest hatch distance of 0.19 mm, exhibited the highest total porosities. Specimens 9-12, printed with the smaller laser spot size, demonstrated the lowest overall total porosities.

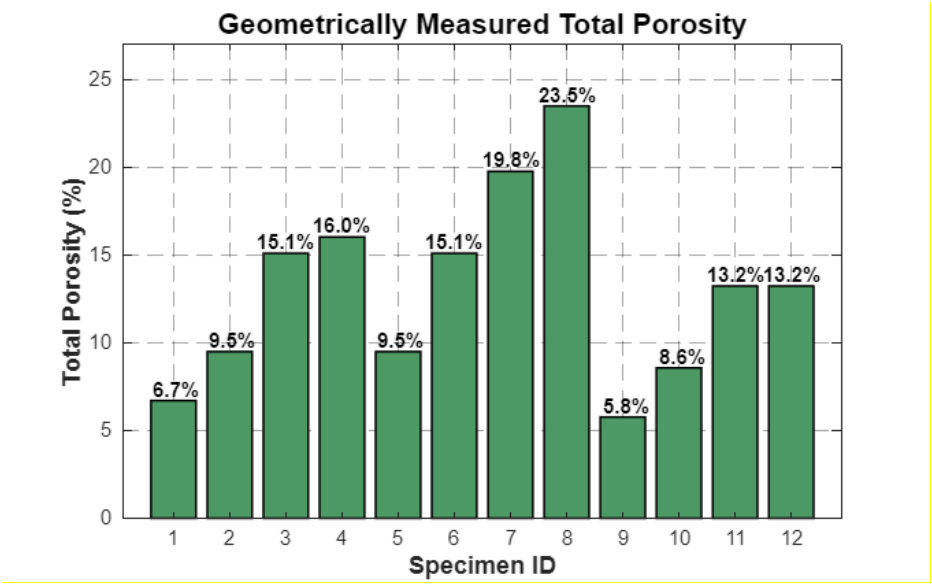

Figure 25. Total porosity of the specimens

4.3 Permeability measurement

The results from gas permeability tests are illustrated in Figure 26. Airflow successfully passed through all specimens. The measured permeability values varied significantly between different parameter sets. Specimens 7 and 8 are tested twice to ensure familiarity with the test setup. The results from the second test runs for these specimens suggest that the initial airflow during the first test might have removed or displaced loose powder trapped inside the pore channels. Specimen 5 exhibited the highest overall permeability.

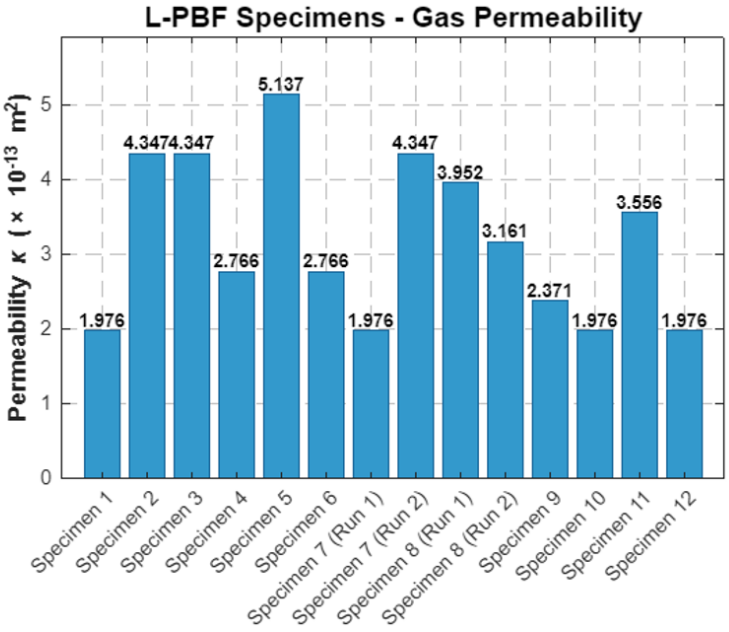

Figure 26. Permeability test results

4.4 Mechanical test results

The tensile stress-strain curves for all the different parameter sets are presented in Figure 27. As anticipated, larger hatch distances corresponded to a lower ultimate tensile strength (UTS). The results for specimens 9–12 indicate that the smaller laser spot size did not have a significant effect on the tensile strength. Specimens 5–8, which are printed with a higher

scanning speed of 1000 mm/s, exhibited the weakest structural integrity. Specimen 8 fractured very early, at a stress level of approximately 100 MPa.

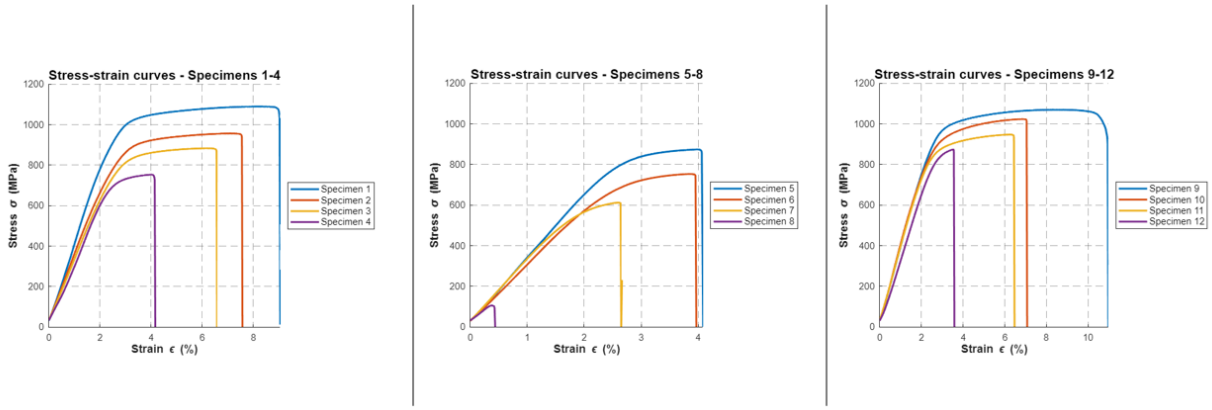

Figure 27. Stress-strain curves for all specimens

The compression test data is presented in Figure 28. Ultimate Compressive Strength (UCS) is not reached by any of the specimens, as the designed cross-sectional area proved to be too large for the 9 kN safety limit of the testing machine. However, the compressive stress-strain curves for specimens 7 and 8 demonstrate that the material's yield limit is successfully reached and exceeded. The curve for specimen 8, exhibits clear plastic deformation, even though the ultimate compression limit could not be achieved before the test is terminated.

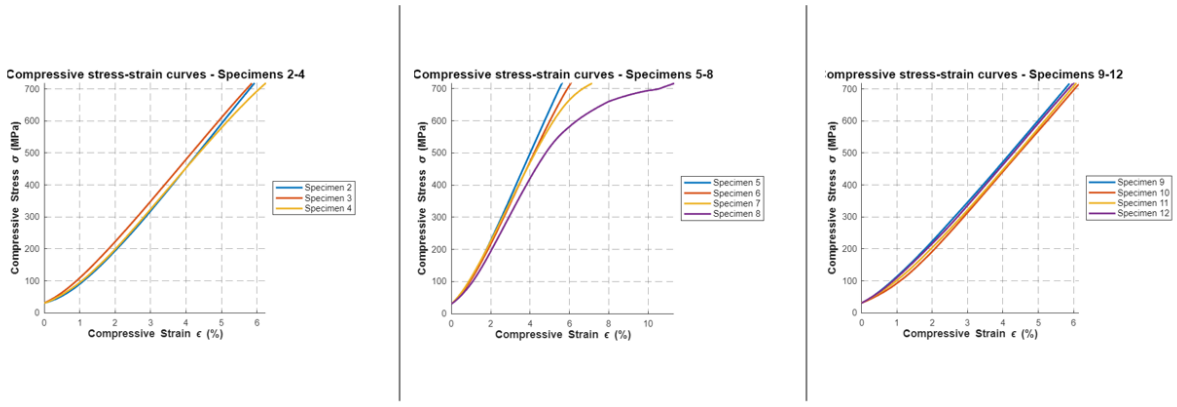

Figure 28. Compressive stress-strain curves

Since the compressive stress-strain curves presented only minor variation between specimens. The compression test results can be expressed in terms of the displacement of the specimens under the 9 kN load. Figure 29 illustrates maximum displacements of compression specimens. Where specimen 8 experienced highest degree of plastic deformation.

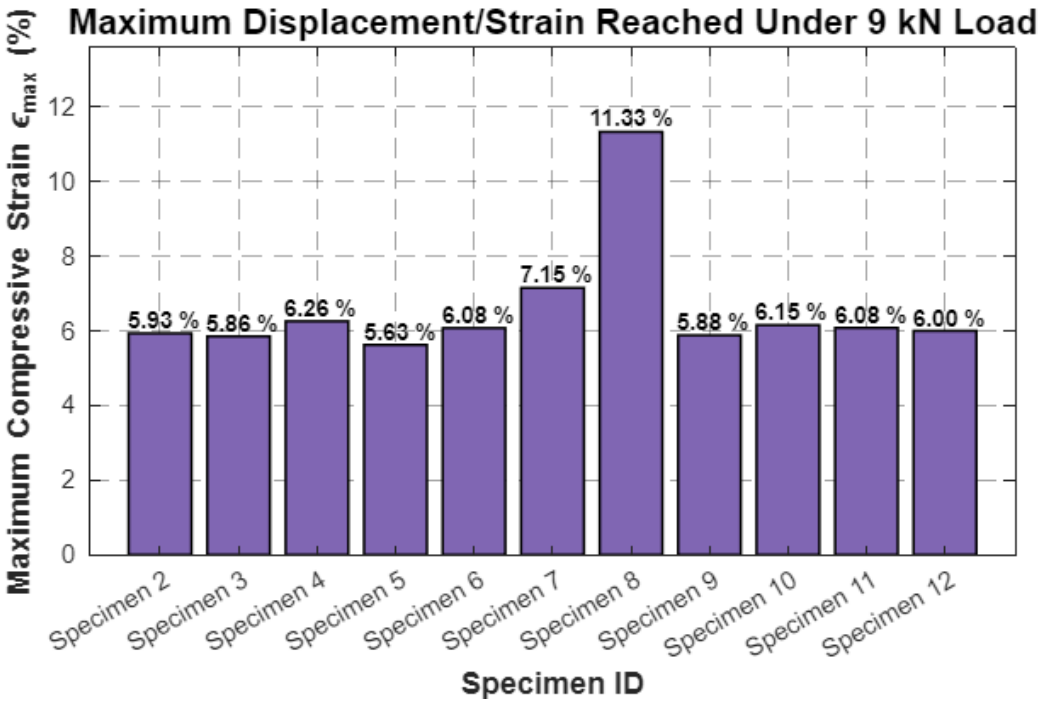

Figure 29. Maximum displacement of compression specimens.

5 Discussion

In this chapter, the results of the research are discussed and analysed in relation to the theoretical framework.

5.1 Combining mechanical results with porosity

The relationship between total porosity and UTS is presented in Figure 30. It is observed that a higher total porosity consistently corresponded to a lower mechanical stress resistance. Specimens 5–8, which are printed with a higher scanning speed of 1000 mm/s, exhibited the weakest tensile strength. The balling effect led to weaker metallurgical bonding between the layers while simultaneously increasing the overall porosity. Specimens 1, 5, and 9 manufactured with the narrowest hatch spacing of 0.13 mm, demonstrated the lowest porosity and the highest mechanical strength. A smaller hatch spacing allows the melt tracks to overlap, creating a denser and structurally stronger component.

A trade-off between porosity and mechanical strength must be accepted when manufacturing porous parts. However, typical industrial applications for highly porous components generally do not require peak mechanical strength characteristics.

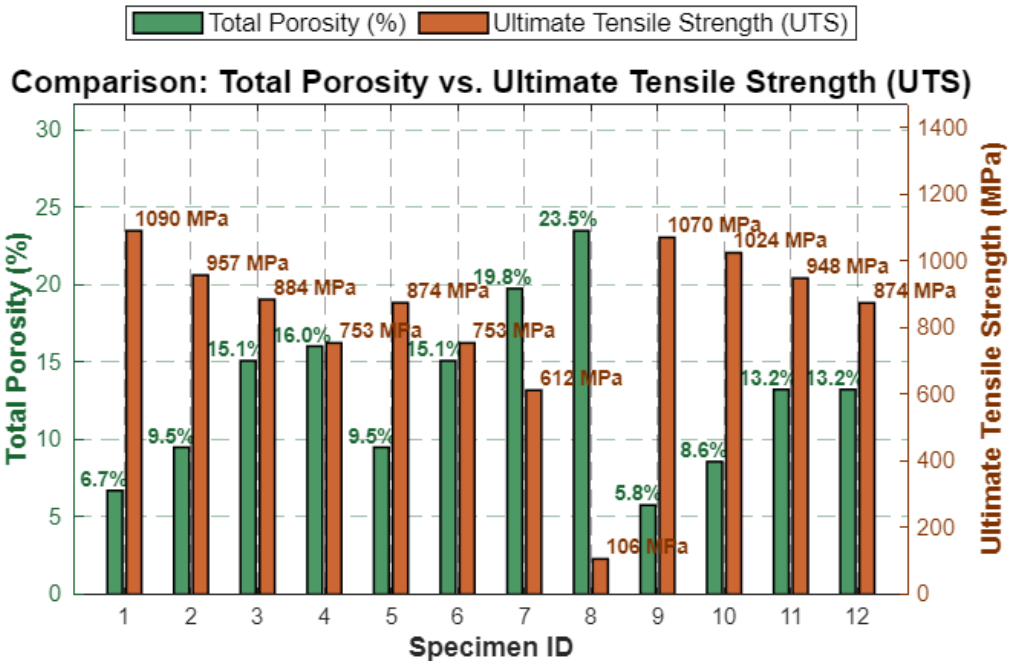

Figure 30. Total porosity vs Ultimate Tensile Strength

5.2 Combining permeability with porosity

The permeability tests did not reveal a direct correlation between higher total porosity and increased gas permeability. Figure 31 shows total porosity with gas permeability. Data shows unexpected as most porous specimen is not the most permeable. The highest gas permeability is observed in specimen 5, despite its relatively low total porosity of 9.5%. Furthermore, specimens 9–12, which are printed with the smaller laser spot size, exhibited both the lowest permeability and the lowest porosity.

The permeability tests are conducted by passing air through the sidewalls of the porous structures. Overall, the specimens manufactured with the largest hatch spacing demonstrated the lowest permeability. A larger hatch spacing leads to wider overhang gaps within the internal porous layers. Molten sidewall structure collapses under these unsupported overhangs, causing the pore channels on the sidewall surfaces to close during the printing process.

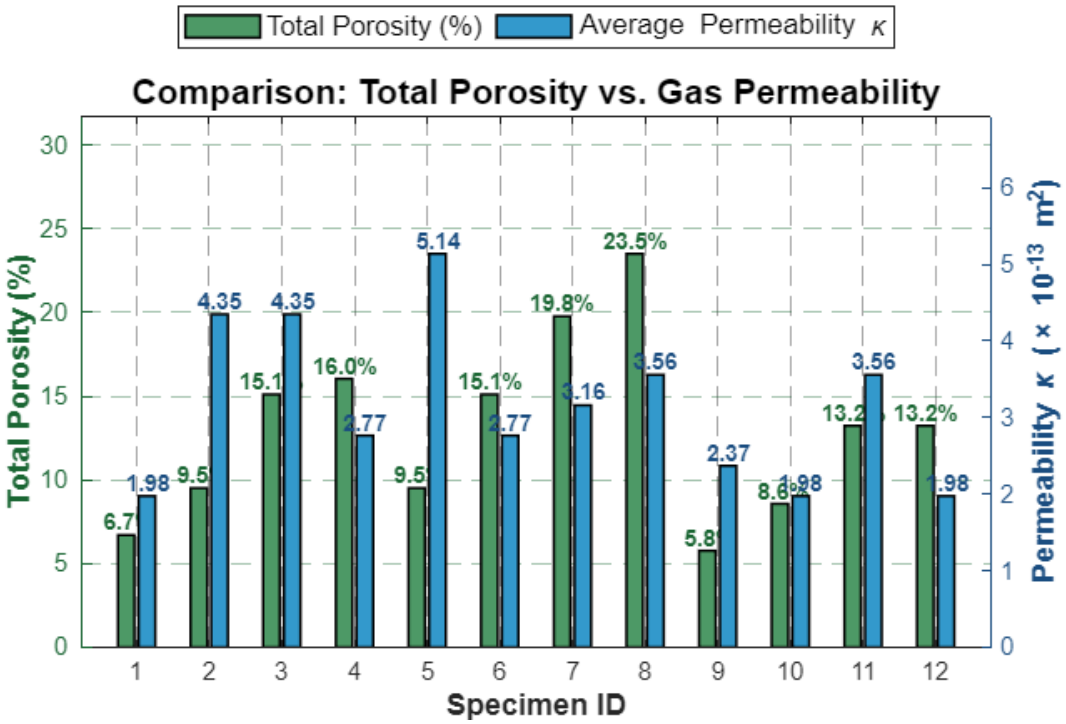

Figure 31. Total porosity with gas permeability

Parameter 5 SEM images in Figure 19 shows lot of porosity and balling phenomena due to increased scanning speed of 1000 mm/s. Even though the hatch spacing is set to the minimum 0.13 mm, the laser-melted tracks did not properly overlap. This lack of overlap is directly caused by the increased scanning speed. Parameter set 8 SEM images in Figure 20 display the highest porosity with the largest visual pores, resulting from the combination of the high scanning speed and the largest hatch spacing 0.19 mm. The severe balling observed in specimens 5 and 8 likely led to an increased number of closed pores, as the surface tension of the rapidly cooling molten metal caused it to form spherical droplets that obstructed the pore channels. Additionally, it remains unknown exactly how much un-melted powder is trapped inside these closed porous structures, which likely contributed to the randomness observed in the permeability results.

5.3 Effect of as-built state into results

All the specimens are in as-built state except half of the SEM cubes. The as-built condition significantly affected the permeability and volume measurement results, as loose and partially sintered powder likely blocked a portion of the internal pore channels. Consequently, these permeability results should be considered indicative, and further examination with cleaned specimens is required to obtain more reliable data.

The mechanical test results may not have reached their full potential, as post-processing could have given better performance. However, evaluating the mechanical properties in the as-built state did not lead into random results. As most porous specimen is weakest and least porous is strongest. Therefore, the as-built condition is not considered to compromise the overall reliability of the mechanical trends, as they aligned perfectly with theoretical assumptions.

5.4 Build orientation effect to porosity

The differences in pore size between the top and side surfaces indicate a clear mechanical and structural anisotropy within the porous components. A larger hatch spacing led to larger pore gaps on the top surface. In the vertical z-direction, the laser melted the underlying layers into a denser structure, rendering the vertical sidewalls significantly less porous compared to the horizontal top surfaces.

Permeability testing through the top surface is excluded from this study, as the solid base support structures are assumed to block the airflow completely. The effect of the build orientation on the porous structure must be carefully considered when designing L-PBF porous parts for various applications. It is highly probable that the permeability in the vertical z-direction would be substantially higher. The SEM images revealed more extensive open pore formation on the top surfaces, which would likely allow more air to pass through compared to the denser, partially collapsed sidewalls. This confirms that the pore characteristics differ fundamentally between the horizontal and vertical build directions.

5.5 Reliability of the test results

The reliability of the test results in this study is constrained by practical manufacturing limitations and time restrictions. There are practical limits on the total number of specimens that could be manufactured. Therefore, the lack of a large sample size for each parameter significantly restricts the statistical reliability of the results.

This thesis mainly highlights the key trends regarding the relationship between porosity and process parameters. A more detailed investigation would have required a significantly larger number of tests. Thus, this study serves as an initial exploration, providing a basis where more in-depth research on specific sub-areas can be continued.

5.6 Further research topics

Further research topics could be post-processing methods to remove loose powder. Loose powder remaining on the surface, and especially trapped inside the porous structure, negatively affects the part's mechanical properties and limits its permeability. Effective powder removal techniques, such as ultrasonic cleaning or abrasive blasting, need to be studied further to optimize filter performance.

A more detailed examination of specific parameter sets using a larger number of identical test specimens is recommended. Future research focusing precisely on one optimal parameter set with multiple repetitions would provide a more statistically reliable characterization of the pore structures.

Non-destructive internal examination of the pore networks should be conducted to determine how they differ from the surface porosity. The use of X-ray micro-computed tomography is highly recommended to visualize the internal 3D architecture of the porous specimens. This would help identify trapped loose powder, reveal how internal pore channels are formed, and provide absolute validation of how process parameters dictate the internal structure of L-PBF parts.

6 Conclusions

This study demonstrates how the twelve tested parameter sets influence the overall porosity and pore characteristics of L-PBF manufactured 15-5 PH stainless steel parts. Due to the limited number of SEM images, specific pore sizes could only be estimated for some of the parameter sets. However, the SEM analysis confirmed clear differences in pore sizes depending on the applied parameters. An increase in the hatch distance resulted in a corresponding increase in both the average pore size and the total porosity, allowing the porosity to be successfully controlled between a minimum of 5.8% and a maximum of 23.5%. The specimens printed with a smaller laser spot size < 75 µm created a more closed sidewall surface structure and the top surface developed narrow and deep pores. Furthermore, the specimens printed with a higher scanning speed of 1000 mm/s are found to be highly porous. The elevated speed induced a severe balling effect and caused the continuous laser melt tracks to break up, which consequently resulted in a high standard deviation in pore sizes. The measured gas permeability of the parts did not strictly correlate with the total geometric porosity.

Mechanically, an increase in the hatch distance consistently led to weaker components. The ultimate tensile strength (UTS) dropped drastically from 1090 MPa for the densest parameter set down to 100 MPa for the most porous specimen. The specimen from parameter sets 1-4 and 9-12 yielded approximately the same ultimate tensile strength, even though the specimens 9-12 printed using the smaller laser spot size.

It is concluded that utilizing intentionally porous L-PBF parts in the as-built state is not optimal for applications such as filtration and flow control. The presence of loose, un-melted powder trapped inside the complex porous structures creates unstable and unpredictable permeability results. Therefore, post-processing methods to effectively clear loose powder from the internal channels require further investigation.

Although practical limitations regarding the number of test specimens and time constraints affected the overall statistical reliability of the results, the primary objectives of the study are successfully achieved within the scope of the experimental phase. Finally, the findings of this research established a strong foundation for understanding parameter driven porosity and highlighted several critical areas for future research.

References

Armstrong, M., Mehrabi, H., & Naveed, N. (2022). An overview of modern metal additive manufacturing technology. *Journal of Manufacturing Processes*, *84*, 1001–1029. Available DOI: 10.1016/j.jmapro.2022.10.060

ASTM. N.d. E8/E8M – 13a. Available: https://www.galvanizeit.com/uploads/ASTM-E-8-yr-13.pdf.

Brennan, M. C., Keist, J. S., & Palmer, T. A. (2021). Defects in Metal Additive Manufacturing Processes. *Journal of Materials Engineering and Performance*, *30*(7), 4808–4818. Available DOI: 10.1007/s11665-021-05919-6

Buhairi, M. A., Foudzi, F. M., Jamhari, F. I., Sulong, A. B., Radzuan, N. A. M., Muhamad, N., Mohamed, I. F., Azman, A. H., Harun, W. S. W., & Al-Furjan, M. S. H. (2023). Review on volumetric energy density: influence on morphology and mechanical properties of Ti6Al4V manufactured via laser powder bed fusion. *Progress in Additive Manufacturing*, *8*(2), 265–283. Available DOI: 10.1007/s40964-022-00328-0

Calignano, F., Cattano, G., Iuliano, L., Manfredi, D. (2018). Controlled Porosity Structures in Aluminum and Titanium Alloys by Selective Laser Melting. In: Meboldt, M., Klahn, C. (eds) Industrializing Additive Manufacturing - Proceedings of Additive Manufacturing in Products and Applications - AMPA2017. AMPA 2017. 181-190. Available DOI: 10.1007/978-3-319-66866-6_18

Chowdhury, S., Yadaiah, N., Prakash, C., Ramakrishna, S., Dixit, S., Gupta, L. R., & Buddhi, D. (2022). Laser powder bed fusion: a state-of-the-art review of the technology, materials, properties & defects, and numerical modelling. *Journal of Materials Research and Technology*, *20*, 2109–2172. Available DOI: 10.1016/j.jmrt.2022.07.121

Du, C., Zhao, Y., Jiang, J., Wang, Q., Wang, H., Li, N., & Sun, J. (2023). Pore defects in Laser Powder Bed Fusion: Formation mechanism, control method, and perspectives. *Journal of Alloys and Compounds*, *944*, Article 169215. Available DOI: 10.1016/j.jallcom.2023.169215

Furumoto, T., Koizumi, A., Alkahari, M. R., Anayama, R., Hosokawa, A., Tanaka, R., & Ueda, T. (2015). Permeability and strength of a porous metal structure fabricated by additive manufacturing. *Journal of Materials Processing Technology*, *219*, 10–16. Available DOI: 10.1016/j.jmatprotec.2014.11.043

Guddati, S., Kiran, A. S. K., Leavy, M., & Ramakrishna, S. (2019). Recent advancements in additive manufacturing technologies for porous material applications. *International Journal of Advanced Manufacturing Technology*, *105*(1–4), 193–215. Available DOI: 10.1007/s00170-019-04116-z

Haiati, S., Dotchev, K., & Lowther, M. (2025). Utilizing Powder Bed Fusion Additive Manufacturing Technology to Fabricate Parts with Controlled Porosity and Permeability Characteristics for Filtration Applications. *International Journal of Precision Engineering and Manufacturing-Green Technology*, *12*(1), 135–149. Available DOI: 10.1007/s40684-024-00636-6

Letenneur, M., Kreitcberg, A., & Brailovski, V. (2019). Optimization of Laser Powder Bed Fusion Processing Using a Combination of Melt Pool Modeling and Design of Experiment Approaches: Density Control. *Journal of Manufacturing and Materials Processing*, *3*(1), 21. Available DOI: 10.3390/jmmp3010021

Oerlikon, MetcoAdd 15-5 PH-A. 2026. Available: https://mymetco-europe.oerlikon.com/en-us/product/metcoadd155pha.

Sardarian, S., Dehgahi, S., Wei, F., Secanell, M., & Qureshi, A. J. (2024). Structured porous 17-PH stainless steel layer fabrication through laser powder bed fusion. *International Journal of Sustainable Engineering*, *17*(1), 306–321. Available DOI: 10.1080/19397038.2024.2334040

Vaglio, E., Scalzo, F., Sortino, M., Totis, G., Cremonese, R., Boccia, M., & Danielis, M. (2024). Optimization of Laser Based-Powder Bed Fusion Parameters for Controlled Porosity in Titanium Alloy Components. *Materials*, *17*(22). Available DOI:10.3390/ma17225572

Wang, W., Ning, J., & Liang, S. Y. (2021). Analytical Prediction of Balling, Lack-of-Fusion and Keyholing Thresholds in Powder Bed Fusion. Applied Sciences, 11(24), 12053. Available DOI: 10.3390/app112412053

Xie, D., & Dittmeyer, R. (2021). Correlations of laser scanning parameters and porous structure properties of permeable materials made by laser-beam powder-bed fusion. *Additive Manufacturing*, *47*, Article 102261. Available DOI: 10.1016/j.addma.2021.102261

Zhang, L., Wang, M., Li, H., & Liu, J. (2025). Research on Mechanical Properties and Permeability of 3D-Printed Permeable Steel by Selective Laser Melting. *Journal of Materials Engineering and Performance*, *34*(14), 15012–15026. Available DOI: 10.1007/s11665-024-10124-2